



Probing the functionality of nanostructured MnCeO_x catalysts in the carbon monoxide oxidation

Part I. Influence of cerium addition on structure and CO oxidation activity

Francesco Arena ^{a,*}, Roberto Di Chio ^a, Barbara Fazio ^b, Claudia Espro ^a, Leone Spiccia ^{c,1}, Alessandra Palella ^d, Lorenzo Spadaro ^d

^a Dipartimento di Ingegneria, Università degli Studi di Messina, Viale F. Stagno D'Alcontres 31, I-98166 S. Agata (Messina), Italy

^b Istituto CNR – Istituto per i Processi Chimico-Fisici, Viale F. Stagno D'Alcontres 37, I-98158 Messina, Italy

^c School of Chemistry, Monash University, Melbourne, 3800, Australia

^d Istituto CNR-ITAE "Nicola Giordano", Via Salita S. Lucia 5, I-98126 S. Lucia (Messina), Italy

ARTICLE INFO

Article history:

Received 27 January 2017

Received in revised form 15 March 2017

Accepted 18 March 2017

Available online 21 March 2017

Keywords:

Nanostructured MnCeO_x catalysts

Structural and electronic effects

CO oxidation

Structure-activity relationships

Active sites

ABSTRACT

The effects of cerium addition on the physico-chemical properties and CO oxidation activity of *nanostructured* MnCeO_x catalysts ($0 \leq c_{\text{Ce}} \leq 1$) have been assessed. Irrespective of the loading, cerium hinders any significant long-range crystalline order promoting surface exposure, oxide dispersion, and reducibility of composite catalysts. Noticeable structural effects and strong oxide interaction lead to different arrangement of the active MnO_x phase, explaining the peculiar reactivity scale of the studied catalysts in the CO oxidation reaction. High activity, good stability, CO₂ productivity values depending on the MnO_x loading, and similar activation energy values in the range of 353–533 K (37–47 kJ/mol) uncover an unchanging reaction mechanism, irrespective of composition and temperature. Although some chemical effects at high Ce loading ($\chi_{\text{Ce}} \geq 0.5$), structure-activity relationships indicate that surface Mn^{IV} centers are the active sites of bulk MnO_x and composite MnCeO_x catalysts.

© 2017 Elsevier B.V. All rights reserved.

1. Introduction

The urgent need to prevent irreversible damages to the environment and natural resources constitutes a major global challenge deserving systematic exploitation of advanced catalytic technologies for environmental safeguard and remediation, *green chemistry* syntheses, and supply of renewable feedstocks, free of CO₂ emissions. Nevertheless, the extensive use of costly noble-metals hinders this technological breakthrough, pressing a big research concern on alternative catalyst formulations based on transition metal oxides (TMO) [1–7].

During the last decades numerous studies documented that bare and promoted manganese oxide catalysts exhibit a performance comparable to supported noble-metals in many liquid and gas phase processes, like the mineralization of toxic-refractory

wastewater by the wet air oxidation (CWAO) [3–6], the oxidative detoxification of gas exhausts [1,3,7–23], the selective NO_x reduction (SCR) [24–29], the synthesis of bio-fuels [30,31] and fine chemicals [9,32–34], the electrochemical oxygen reduction (ORR) [35,36] and water oxidation [37,38]. That is because MnO_x materials ($x > 1$) exhibit excellent redox activity and O₂-activation functionality, further tuneable by promoters' addition. In particular, cerium effectively promotes reactivity and chemical stability of MnO_x catalysts, although oxide dispersion and interaction pattern affect structure and reactivity of composite MnCeO_x materials [3]. Thus, special synthesis routes have been devised to improve the functionality of MnCeO_x systems [3,9,11,22,23,39–42], while recent computational studies addressed physico-chemical and catalytic properties of surface Mn ions adsorbed on ceria surface [43,44]. Despite quanto-chemical evidences on model systems predict high mobility of oxygen-bridge species and a superior O₂-activation capability of the Mn-doped ceria surface [43,44], structural and/or electronic effects shape the functionality of "real" MnCeO_x catalysts [3,9,11,22,32,34]. In particular, compositions corresponding to manganese-to-cerium atomic ratios in between 0.3

* Corresponding author at: Dipartimento di Ingegneria, Università degli Studi di Messina, Italy.

E-mail address: Francesco.Arena@unime.it (F. Arena).

¹ Deceased on Dec. 18th, 2016.

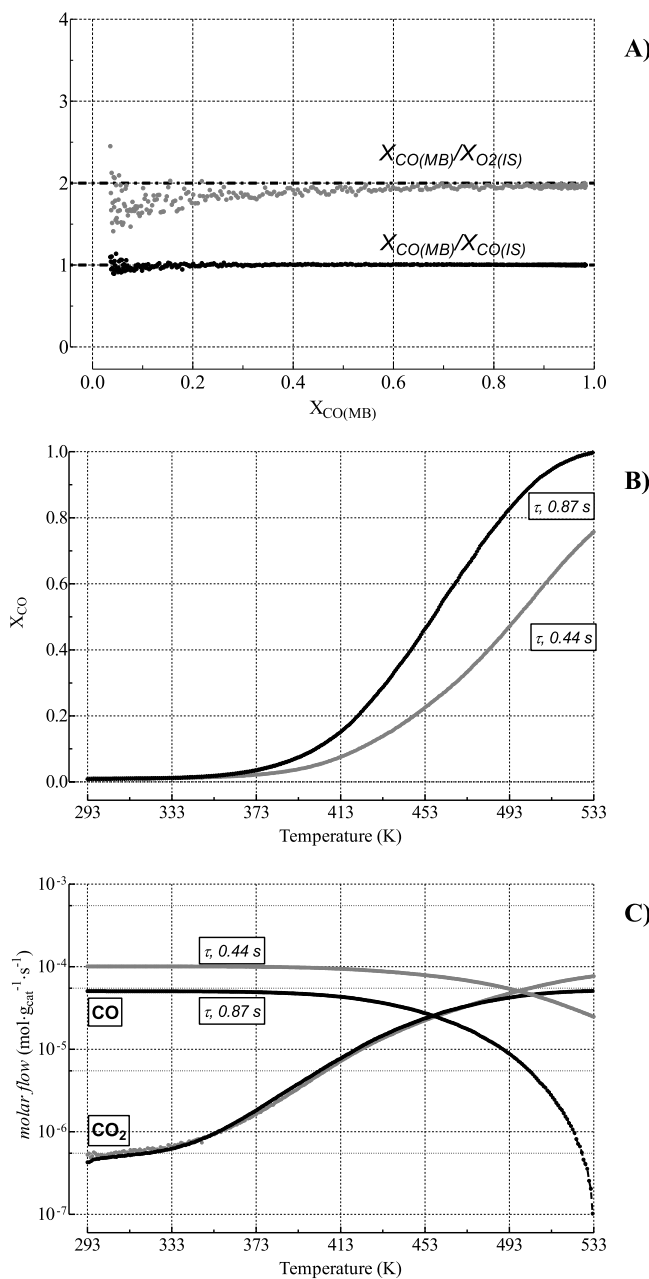


Fig. 1. (A) Comparison of CO conversion data by internal-standard and mass-balance methods ($X_{CO(MB)}/X_{CO(IS)}$) and CO-O₂ conversion values ($X_{CO(MB)}/X_{O_2(IS)}$) as function of X_{CO} ; Influence of the contact time on (B) CO conversion and (C) CO_x molar flow. (Catalyst, M5C1; w_{cat} , 0.02 g; F, 60–120 stp mL/min; P, 1 atm; p_{CO} , 0.025; p_{O_2} , 0.025).

and 2.0 generally ensure the best performance [3,9,11,22,23,45], while highly Mn-loaded catalysts have been scarcely investigated also in spite of the economic advantages due to lower cerium content in catalyst formulation [46].

Therefore, this study is aimed at relating thoroughly physicochemical properties and CO oxidation functionality of nanostructured MnCeO_x catalysts ($0 \leq x \leq 1$) synthesized via the *redox-precipitation route* [32,37,42]. Improved surface area, oxide dispersion and redox behavior signal remarkable structural effects in nanostructured MnCeO_x catalysts, while basic structure-activity relationships shed light into the nature of active sites providing evidence of some peculiar chemical effects at high Ce loading ($x \geq 0.5$).

2. Experimental

2.1. Catalyst preparation

Bare (M) and cerium (MxCy) promoted MnO_x catalysts with different atomic ratios (Mn/Ce, x/y) were prepared via the acidic protocol of the *redox-precipitation route* [32,42]. Deionized water (0.1 L) at pH ≈ 4.5 (adjusted by HNO₃ addition) was heated at 343 K under stirring and nitrogen flow to remove dissolved oxygen. Then, proper amounts of the Mn(NO₃)₂·4H₂O (>97%, Carlo Erba) precursor were solubilized therein and titrated by dropwise addition of an aqueous solution (0.15 L) of the KMnO₄ (≥99%, Carlo Erba) and Ce(NH₃)₂(NO₃)₆ (>98.5%, Aldrich) precursors (pH ≈ 1). During titration, the pH was kept constant (4.5 ± 0.5) by the addition of KOH solution (0.1 M), forcing the following *redox-precipitation* reactions

The bare CeO₂ (C) sample was obtained by precipitation of the above ceria precursor at pH of 4.5. Thereafter the solids were digested, filtered, washed, dried at 373 K (16 h) and calcined at 673 K (6 h). The list of the catalysts, with the relative code and the main physico-chemical properties, is presented in Table 1.

2.2. Catalyst characterization

X-ray fluorescence (XRF) analyses were performed by a Bruker AXS-S4 Explorer spectrometer, taking the K_{α1} emission to determine the chemical composition of the catalysts.

N₂-physisorption isotherms were obtained at 77 K using an ASAP 2010 static adsorption device (Micromeritics Instrument). Surface area (SA), pore volume (PV), and average pore diameter (APD) data were obtained by elaboration of isotherms by BET and BJH methods.

X-ray diffraction (XRD) analyses in the range of 10–80° were performed by a Philips X-Pert diffractometer using Ni β-filtered Cu K_α radiation (40 kV; 30 mA) with a scan rate of 0.05°/min.

Raman Spectroscopy (RS) analyses were performed using a laser wavelength of 632.8 nm (He-Ne) at a power of 0.03 mW, focused on the sample by a 50× objective at long focal distance over a 1.5 μm diameter spot. Measurements were carried out on the “as prepared” samples, and after laser annealing at higher laser power (3 mW; 30 s) under the same conditions. The signal, collected by a microscope (Olympus BX41) in the back-scattering configuration, was dispersed by a HR800 monochromator (Horiba-Jobin Yvon) and detected by a Peltier-cooled silicon charge-coupled device (CCD) array sensor (Synapse, Horiba-Jobin Yvon), with a resolution of ≈3 cm⁻¹.

X-ray Photoelectron Spectroscopy (XPS) data were obtained using a Physical Electronics GMBH PHI 5800-01 spectrometer operating with a monochromatized Al-K_α radiation with a power beam of 300 W. The pass energy for determination of the oxidation state and concentration of surface species was 11.0 eV and 58.0 eV, respectively. The BE regions of C_{1s}-K_{1s} (280–300 eV), Mn_{2p} (635–680 eV), Ce_{3d} (870–935 eV), and O_{1s} (525–535 eV) were investigated, taking the C_{1s} line (284.8 eV) of adventitious carbon as reference.

Temperature Programmed Reduction (TPR) measurements in the range of 293–773 K were carried out using a linear quartz microreactor (i.d., 4 mm), heated at the rate of 12 K/min and fed with a 5% CO/He (CO-TPR) carrier flowing at 60 stpmL/min. The analyses were performed using catalyst samples of 20 mg after a pretreatment in situ under a 5% O₂/He flow at 423 K (1 h). The CO consumptions was monitored by a TCD after removing water and carbon dioxide by a trap containing Mn(ClO₄)₂ and ascarite, respectively [32].

2.3. Catalyst testing

CO oxidation activity has been probed by temperature programmed catalytic reaction (TPCR) measurements in the range of 293–533 K, using the above microreactor heated at the rate of

Table 1

Physico-chemical properties of the studied catalysts.

Catalyst	Bulk Composition						SA (m^2/g)	PV (cm^3/g)	APD (nm)		
	(wt%) ^a				(at%)						
	MnO_x	CeO_x	KO_x	Mn	Ce	K	χ_{Ce}				
C	—	100	—	—	100	—	1.00	132	0.10		
M1C3	14.1	85.8	0.1	24.2	75.5	0.3	0.75	204	0.55		
M1C1	34.4	65.4	0.2	50.7	48.8	0.5	0.50	190	0.46		
M3C1	59.9	36.8	3.2	70.8	22.0	7.2	0.24	184	0.57		
M5C1	66.9	28.4	4.7	74.3	16.0	9.7	0.18	159	0.56		
M9C1	77.0	17.6	5.4	80.3	9.3	10.4	0.10	136	0.49		
M	93.5	—	6.5	88.6	0.0	11.4	0.00	94	0.34		

^a Calculated as MnO_2 , CeO_2 and K_2O .

4 K/min. A $\text{CO}/\text{O}_2/\text{He}$ (1/1/38) mixture ($p_{\text{CO}} = p_{\text{O}_2}$, 0.025 atm; P , 1 atm) was fed at the rate of 60 stp $\text{ml}\cdot\text{min}^{-1}$ on 20 mg powdered catalyst samples ($d_p < 0.05 \text{ mm}$) diluted (1/15, wt/wt) with granular SiC ($L_b \approx 20 \text{ mm}$), controlling the temperature by a K-type thermocouple in contact with the catalyst bed. Before tests, all the catalysts were pretreated under a 5% O_2/He flow at 423 K (1 h). The reaction stream was analysed *on line* by a HPR 20 QMS (Hiden Analytical), acquiring the signals of He, H_2O , CO, O_2 , and CO_2 in *Multiple Ion Detection* (MID) mode. With He as internal standard, conversion values calculated by the *internal standard* (X_{IS}) and *mass balance* (X_{MB}) methods

$$X_{\text{IS}} = 1 - \frac{(p_{\text{CO}}/p_{\text{He}})_T}{(p_{\text{CO}}/p_{\text{He}})_{293\text{K}}} \quad (1)$$

$$X_{\text{MB}} = \frac{(p_{\text{CO}_2})_T}{(p_{\text{CO}} + p_{\text{CO}_2})_T} \quad (2)$$

showed good agreement ($\pm 5\%$) and data reproducibility ($> 95\%$).

3. Results and discussion

3.1. Effects of cerium on the CO oxidation activity of MnCeO_x catalysts

The reactivity pattern of the studied systems in the CO oxidation was systematically probed by temperature programmed reaction measurements (TPCR) in the range of 293–533 K [47,48].

Consistency and accuracy of tests are preliminarily documented by representative experimental results of the M5C1 catalyst in Fig. 1. In particular, the reliability of conversion data is evident from good agreement between mass-balance and internal-standard conversion data ($X_{\text{CO}(\text{MB})}/X_{\text{CO}(\text{IS})}$, 1) and stoichiometric $\text{CO}-\text{O}_2$ conversion values ($X_{\text{CO}(\text{MB})}/X_{\text{O}_2(\text{IS})}$, 2) in the X_{CO} range of 3–100% (Fig. 1A). Furthermore, very low reagents concentration (2.5%), powdered catalyst samples ($d_p < 5 \cdot 10^{-5} \text{ m}$) and proper reactor configuration ($d_{\text{int}}, 4 \cdot 10^{-3} \text{ m}; L_b \approx 2 \cdot 10^{-2} \text{ m}$) ensure the kinetic regime of the tests. Indeed, theoretical calculations rule out mass-transfer resistances by internal-external diffusion and axial dispersion phenomena for the most active M catalyst, even at conversion level of 80% (App. A of SI). This is experimentally confirmed by proportional changes in X_{CO} (Fig. 1B) and unchanging CO_2 yields in the range of 293–513 K (Fig. 1C), recorded at different contact time for the M5C1 catalyst. In particular, productivity values between $5 \cdot 10^{-7}$ and $5 \cdot 10^{-5} \text{ mol CO}_2 \text{ g}_{\text{cat}} \text{ s}^{-1}$ well compare with recent literature data of bare and promoted MnO_x catalysts, summarized in Table 2.

At variance with the total inactivity of the SiC material (BT) and the very poor performance of ceria (C), starting to be active at 433 K and reaching a final CO conversion of 15% (533 K), bulk and promoted MnO_x catalysts trigger the formation of CO_2 already at 293 K, attaining final X_{CO} between 75 and 100% (Fig. 2A). In particular, M1C1 and bulk M materials are the most active catalysts featuring a full CO conversion at 533 K and 513 K respectively, while the M3C1 and M5C1 ones show lower activity levels, although higher than the least active M1C3 system.

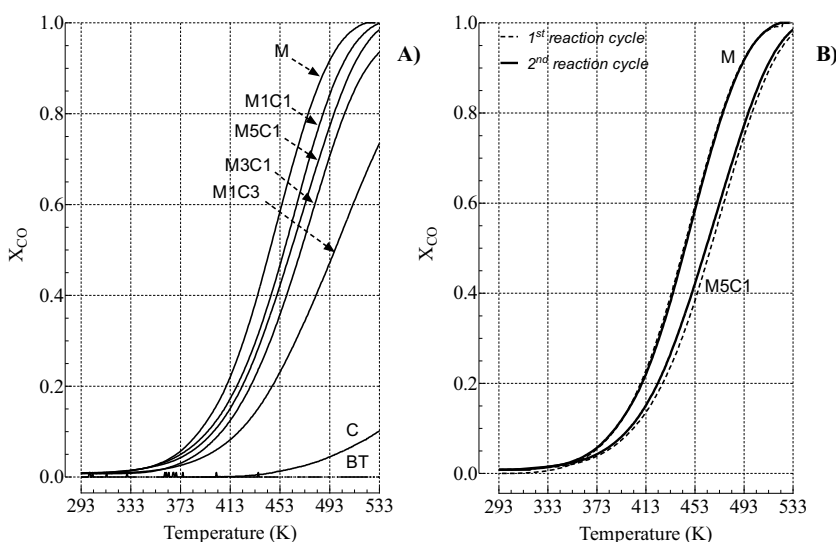
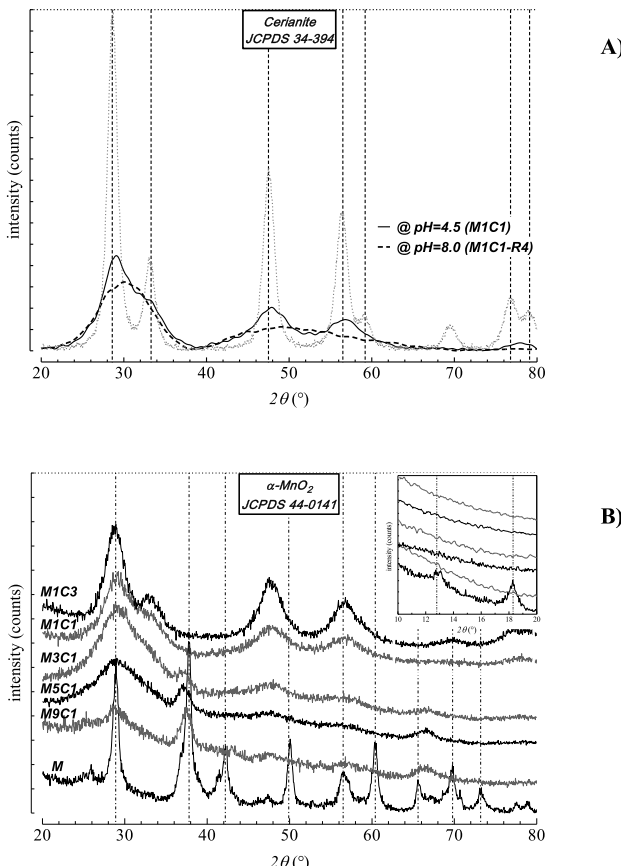


Fig. 2. (A) CO conversion of the studied catalysts in the range of 293–533 K; (B) Stability test of M5C1 and M catalysts. (F , 60 stp mL/min ; P , 1 atm; p_{CO} , 0.025; p_{O_2} , 0.025; w_{cat} , 0.02 g).

Table 2Literature CO₂ yield data of bare and promoted MnO_x catalysts at various temperatures.

Catalyst Composition	F (mL/min)	Reaction mixture composition (%)	W _{cat} (g)	F _{mol} (mol _{CO} g _{cat} ⁻¹ s ⁻¹)	X _{CO} ^b (%)	Y _{CO2} ^b (mol _{CO2} g _{cat} ⁻¹ s ⁻¹)	T ^b (K)	Ref.
MnO _x	50	CO (2.0) – O ₂ (2.0) – Ar (96.0)	0.14	5.0·10 ⁻⁶	≈14	7.0·10 ⁻⁷	≈298	[8]
MnO _x	50	CO (2.0) – O ₂ (2.0) – Ar (96.0)	0.14	5.0·10 ⁻⁶	100	5.0·10 ⁻⁶	≈423	[8]
Mn _{0.5} Ce _{0.5} O _x	10	CO (1.0) – Air (99.0)	0.03	2.3·10 ⁻⁶	100	2.3·10 ⁻⁶	≈373	[9]
Pr _{0.8} Ba _{0.2} MnO _{3-δ}	50 ^a	CO (0.2) – O ₂ (10.0) – He (89.8)	0.10	6.9·10 ⁻⁷	100	6.9·10 ⁻⁷	≈443	[10]
Mn _{0.5} Ce _{0.5} O _x	100	CO (8.0) – O ₂ (4.0) – He (88.0)	0.03	1.8·10 ⁻⁴	≈2	2.9·10 ⁻⁶	373	[11]
Mn _{0.5} Ce _{0.5} O _x	100	CO (8.0) – O ₂ (4.0) – He (88.0)	0.03	1.8·10 ⁻⁴	≈4	5.9·10 ⁻⁶	393	[11]
Mn _{0.5} Ce _{0.5} O _x	100	CO (8.0) – O ₂ (4.0) – He (88.0)	0.03	1.8·10 ⁻⁴	≈9	1.4·10 ⁻⁵	423	[11]
CuMnO _x	22.5	CO (1.0) – O ₂ (89.0) – He (10.0)	0.10	1.6·10 ⁻⁶	25	4.0·10 ⁻⁷	298	[18]
Au/CuMnO _x	22.5	CO (1.0) – O ₂ (89.0) – He (10.0)	0.10	1.6·10 ⁻⁶	55	8.8·10 ⁻⁷	298	[18]
MnO ₂	200	CO (1.0) – O ₂ (4.0) – N ₂ (95.0)	0.10	1.4·10 ⁻⁵	100	1.4·10 ⁻⁵	≈473	[19]
Mn _{0.3} Ce _{0.7} O _x	50–60	CO (1.0) – O ₂ (1.0) – Ar (98.0)	0.10	4.2·10 ⁻⁶	100	4.2·10 ⁻⁶	≈473	[21]
Mn _{0.5} Ce _{0.5} O _x	50	CO (1.0) – O ₂ (20.0) – Ar (79.0)	0.05	6.9·10 ⁻⁶	100	6.9·10 ⁻⁶	463	[22]
Mn _{0.4} Ce _{0.6} O _x	250 ^a	CO (2.0) – O ₂ (10.0) – N ₂ (88.0)	0.50	6.9·10 ⁻⁶	100	6.9·10 ⁻⁶	≈393	[13]

^a From GHSV values assuming a catalyst density of 1 g/cm³.^b CO conversion, CO₂ yield and relative temperature.**Fig. 3.** (A) XRD patterns of the MnCeO_x (Mn_{at}/Ce_{at}, 1) catalyst synthesized via the redox-precipitation route at acidic (M1C1) and basic pH (M1C1-R4) [ref. [11]]; (B) XRD pattern of the studied catalysts.

Catalyst stability was also ascertained by a 2nd consecutive TPCR test on M and M5C1 catalysts, without any intermediate treatment after the 1st reaction cycle. Experimental results in Fig. 2B show an unchanging activity irrespective of composition proving, at once, good catalyst stability [11] and data reproducibility [47,48].

Therefore, catalyst screening indicates that the reactivity of composite MnCeO_x materials is mostly determined by the functionality of the MnO_x phase, according to our recent findings in the selective aerobic oxidation of benzylic alcohol [32], and the promoting effect of Mn^{IV} oxo-complexes on the CO oxidation activity of ceria predicted by computational studies [43,44].

3.2. Effects of cerium on the structure of MnCeO_x catalysts

In previous works we have shown that the redox-precipitation route ensures very high oxide dispersion, resulting in the lack of significant long-range crystalline order in nanocomposite MnCeO_x materials [11,22,30–32,39–42]. However, XRD analysis of the redox-precipitated MnCeO_x (Mn_{at}/Ce_{at}, 1) material obtained at acidic (M1C1) and basic pH (M1C1-R4) discovers that the former protocol somewhat favours the crystallinity of the cerianite phase (Fig. 3A), this being even more evident for M1C3 catalyst (Fig. 3B). Likely consequence of the Ce^{IV} precursor used instead of Ce^{III} one [11,32,41,42], yet, the Sherrer's equation indicates a ceria particle size still in the order of few nanometers, decreasing with Ce loading (2–3 nm). Indeed, a particle size smaller than pure ceria (5–6 nm) confirms that Mn-addition hinders the growth of ceria crystallites [23]. Further, while no MnO_x phases are detectable in M1C3 and M1C1 samples, the lessening of ceria signals and the progressive growth of a peak at ca. 37.5° reveal the incipient formation of MnO₂ nanodomains at lower cerium loading ($\chi_{\text{Ce}} < 0.5$). At variance, the bulk M sample shows several lines in the whole 2θ range, matching the pattern of the body-centred tetragonal α-MnO₂ phase that includes K⁺ ions in the tunnel structure parallel to c-axis [17,20,36,50]. Chemical analysis data indicate a consistent K/Mn atomic ratio of 0.12–0.13 [36], similarly to composite catalysts with $\chi_{\text{Ce}} \leq 0.25$, while potassium is virtually absent at higher cerium loading (Table 1).

While ruling out the presence of crystalline structures in composite MnCeO_x systems obtained at basic pH [11,41,51], Raman spectroscopy is in this case useful to assess the structure of the oxide nanodomains probed by XRD analysis. In particular, the RS spectra in Fig. 4 show for the bulk M sample three main peaks at 187, 584 and 635 cm⁻¹ that are characteristic of MnO₂ phase(s), although their definitive assignment is rather controversial [17,36,50–52]. Indeed, the RS spectrum of the β-MnO₂ phase obtained by BTEM (band-target entropy minimization) analysis matches the above pattern both in peak position and intensity ratio [52], while Gao et al. argued that bands at 574 and 634 cm⁻¹ are rather diagnostic of a tetragonal, hollandite-type, framework (e.g., cryptomelane) [50]. Overall, these evidences suggest that the M sample consists of nanodomains of the K-MnO₂ phase, although a crucial “precursor-concentration” effect, leading to stabilization of α/β MnO₂ phases [17], might explain the different structure of MnO_x samples recently obtained via the same synthesis protocol [32,37]. The RS spectra of composite materials with low Ce loading ($\chi_{\text{Ce}} < 0.5$) miss the peak at 187 cm⁻¹, while the other two signals shift to lower and higher wavenumbers respectively, likely as a consequence of the defective nature of MnO₂ nanodomains [49–52]. These disappear at higher Ce loading ($\chi_{\text{Ce}} \geq 0.5$), while

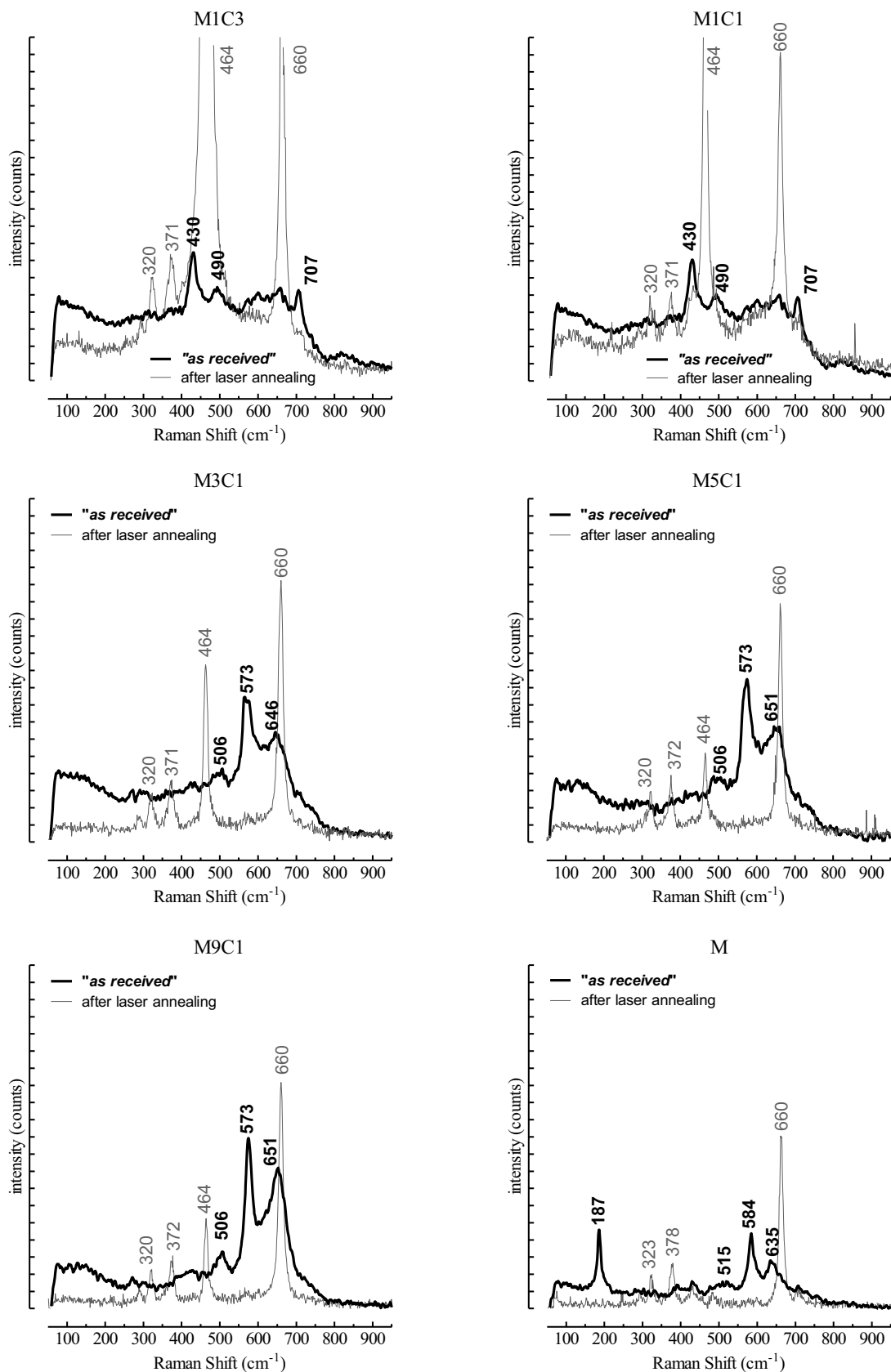


Fig. 4. Raman scattering spectra of the studied catalysts.

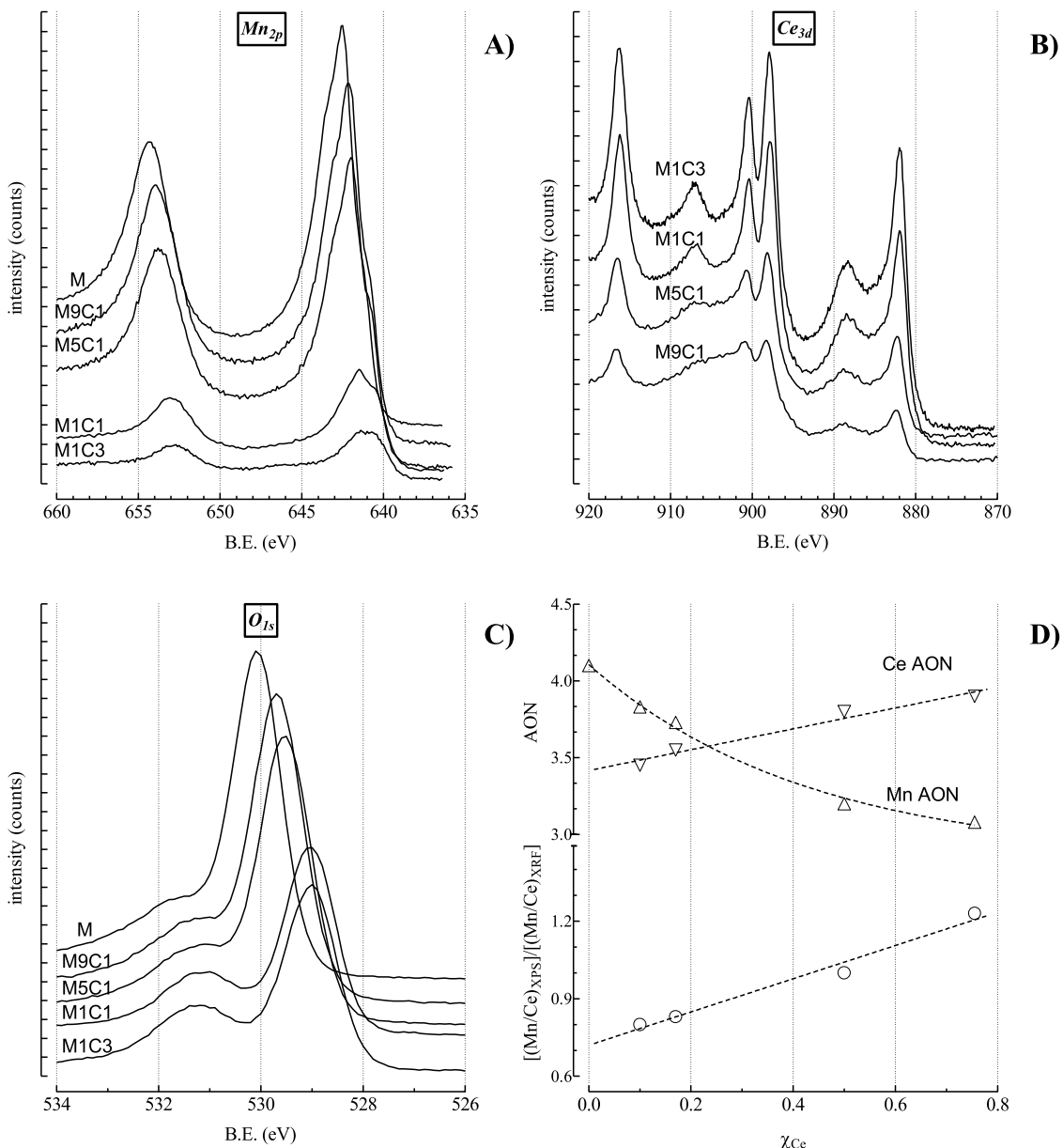


Fig. 5. XPS spectra of Mn_{2p} (A), Ce_{3d} (B) and O_{1s} (C) core levels, and effect of cerium loading on the AON and relative abundance of surface Mn and Ce atoms (D).

some other peaks (430, 490, 707 cm⁻¹) become evident (Fig. 4). Their occurrence in the spectrum of pure ceria (Fig. S1) actually suggests that they could arise from the O-Ce-O stretching in very defective nanoparticles [53], although it must be stressed that similar shifts of the *F*_{2g} cerianite peak [54,55] and absence of Mn-O fingerprints in the range of 620–660 cm⁻¹ [49] were ascribed to surface and sub-surface solid solution(s) in MnCeO_x materials with high Ce content [9,49,54,55].

On the other hand, new signals at 320, 375, and 660 cm⁻¹ of the Mn₃O₄ compound, and the canonical *F*_{2g} peak of cerianite (464 cm⁻¹) confirm a deep structure reorganization of the samples further to laser-annealing [51,52].

The structural effects of the promoter are also evident from the textural properties of the studied catalysts (Table 1). These feature “H1” physical nitrogen adsorption isotherms, typical of mesoporous materials with fairly uniform pore size distribution (Fig. S2), accounting for SA values rising asymptotically from 136 (M9C1) to 204 m²/g (M1C3), and considerably larger than C (132 m²/g) and M (94 m²/g) materials. Larger surface exposure than co-precipitated

[45], and redox-precipitated materials at basic pH [11,39], confirm a remarkable influence of the synthesis route on catalyst texture (Fig. S3). However, PV and APD comparable to M sample and much larger than ceria indicate that an outer shell of MnO_x phase(s) determine the morphological features of *nanostructured* MnCeO_x materials (Fig. S3) [11,32].

In conclusion, quasi-molecular dispersion and strong oxide interaction stabilise poorly crystalline MnO_x phases and surface Mn-O-Ce solid solution at high Ce loading [9,17,21,22,32,36,54,55], hindering the crystallization of MnO₂ in composite catalysts with low Ce loading ($\chi_{\text{Ce}} < 0.5$).

3.3. Effects of cerium on surface chemistry and reducibility of MnCeO_x catalysts

The XPS spectra of Mn_{2p}, Ce_{3d} and O_{1s} core levels and the influence of Ce loading on average oxidation number (AON) and relative abundance of surface Mn and Ce atoms are shown in Fig. 5, while

position and splitting values of Mn_{2p} peaks and surface composition data of the studied catalysts are summarized in Table S4.

All Mn_{2p} spectra (Fig. 5A) feature the typical 2p_{1/2} (652.8–654.3 eV) and 2p_{3/2} (641.4–642.5 eV) signals, shifting upward and resulting in spin-orbit split (ΔE_s) growing at lower X_{Ce} (Table S3). In particular, bulk (M) and composite catalysts with low Ce content (M5C1, M9C1) feature a similar split (11.7–11.8 eV) that is characteristic of MnO₂ species [9,21,36], while lower ΔE_s values (11.4–11.5 eV) indicate oxidation states close to III at high Ce content (M1C3, M1C1), in agreement with the AON decrease probed by the maximum position of 2p_{3/2} peak (Fig. 5D) [11]. The Ce_{3d} spectra are rather complex, due to the evident contribution of six transitions relative to Ce^{IV} and four hidden components of Ce^{III} ions (Fig. 5B) [11,21,23,56]. Taking the transition at 916.3 eV as characteristic of the IV state [11,56], deconvolution analysis provides AON's rising from 3.5 (M9C1) to 3.9 (M1C3) resulting, thus, in a trend opposite to that of Mn atoms (Fig. 5D). Furthermore, all the O_{1s} spectra (Fig. 5C) show a main peak shifting from 529.1 (M1C3, M1C1) to 530.2 eV (M), attributable to lattice ions (O_I), along with a smaller component at higher B.E. keeping a same position (531.3–531.5 eV) that is generally ascribed to surface hydroxyls and/or adsorbed oxygen species (O_{II}) [11,36,49,56]. In fact, the significant shift of the O_I component mirrors the different surrounding of lattice oxygen, considering that abundance of cerium atoms and the strong CeO_x-MnO_x interaction in M1C3 and M1C1 catalysts account for B.E. values typical of ceria [11,49], while increasing concentrations of Mn-O bonds lead to its progressive upward shift at low Ce loading. Actually, higher B.E. could be diagnostic of lower electron density of the O_I species of the MnO_x phase substantiating, in turn, a higher oxidation strength of Mn^{IV} ions than Ce^{IV} ones. This partial electron-withdrawal enhances the electrophilic character of surface oxygen species, determining a superior reactivity of the bulk M system than C one (Fig. 2A). On the other hand, the higher intensity of the O_{II} peak matches larger surface area, and probably exposure of defect sites, in M1C3 and M1C1 samples.

Although it could be argued that the XPS photoelectron sampling depth (2–3 nm) compares to the size of oxide nanodomains, the concentration ratio of Mn and Ce atoms at surface and in the bulk, [(Mn/Ce)_{XPS}]/[(Mn/Ce)_{XRF}], depicts a rising trend with X_{Ce} (Fig. 5D), being at variance with the unchanging surface Mn enrichment recorded for redox-precipitated samples at basic pH [11,39,41,42]. A decrease from 1.23 to 0.80 mirrors, in fact, the incipient MnO₂ crystallization occurring at low Ce loading, and the incorporation of Mn ions with lower oxidation state in the defective positions of ceria nanoparticles (surface solid solutions) in M1C3 and M1C1 samples [9,21,34]. Finally, XPS data typical of K-MnO₂ species are found for the bulk M sample [36].

The catalyst reducibility has been probed by CO-TPR measurements, shedding also light into the reactivity of catalyst oxygen toward the reaction substrate [32]. All the reduction profiles in Fig. 6 consist of a main peak, with maximum shifting from 453 (M1C1) to 533K (M), merged with a smaller component that keeps an unchanged maximum position (607K), except for the bulk M sample (648K). In particular, the peak at low temperature, due to surface Mn^{IV} centers, constitutes the prevailing portion of the reduction profile in agreement with high MnO_x dispersion, while the 2nd peak mostly monitors the bulk reduction of MnO_x phases ($x \leq 1.5$) [32]. In particular, an onset temperature close to 293K irrespective of composition signals a similar high reactivity of surface Mn^{IV} sites to CO and, consequently, minor chemical effects of the promoter. Therefore, the easier reduction of composite catalysts is mainly due to the *structural effects* of cerium promoting MnO_x dispersion [32]. Hence, extents of CO consumption roughly proportional to MnO_x loading (CO/Mn, 0.87–1.03) account for the reduction of MnO_x phases to MnO in bulk and composite catalysts

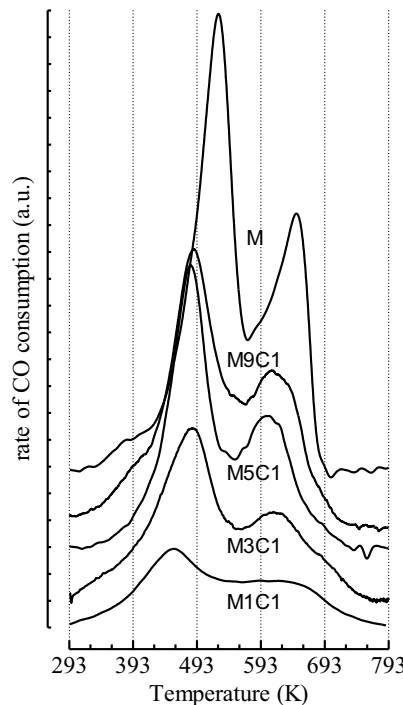


Fig. 6. CO-TPR pattern of the studied catalysts.

with low Ce loading, signaling the reduction of a significant fraction of surface Ce^{IV} ions in M1C3 and M1C1 catalysts [32,43,44].

3.4. Mechanistic clues and structure-activity relationships

Further insights into the effects of promoter and temperature on mechanism and kinetics of the CO oxidation are given by the apparent activation energy values listed in Table 3. These were obtained from the Arrhenius plot of differential conversion data (X_{CO}, 3–10%; T, 353–423K) and the analysis of integral data (X_{CO}, 3–80%; T, 353–533K) by the pseudo-1st order kinetic equation for catalytic oxidations in packed-bed reactor [57], being a realistic hypothesis in view of further kinetic evidences [58],

$$\ln[-\ln(1-X)] = \ln(a) + \ln(\tau) - \left(\frac{E_{app}}{R}\right) \cdot \frac{1}{T} \quad (3)$$

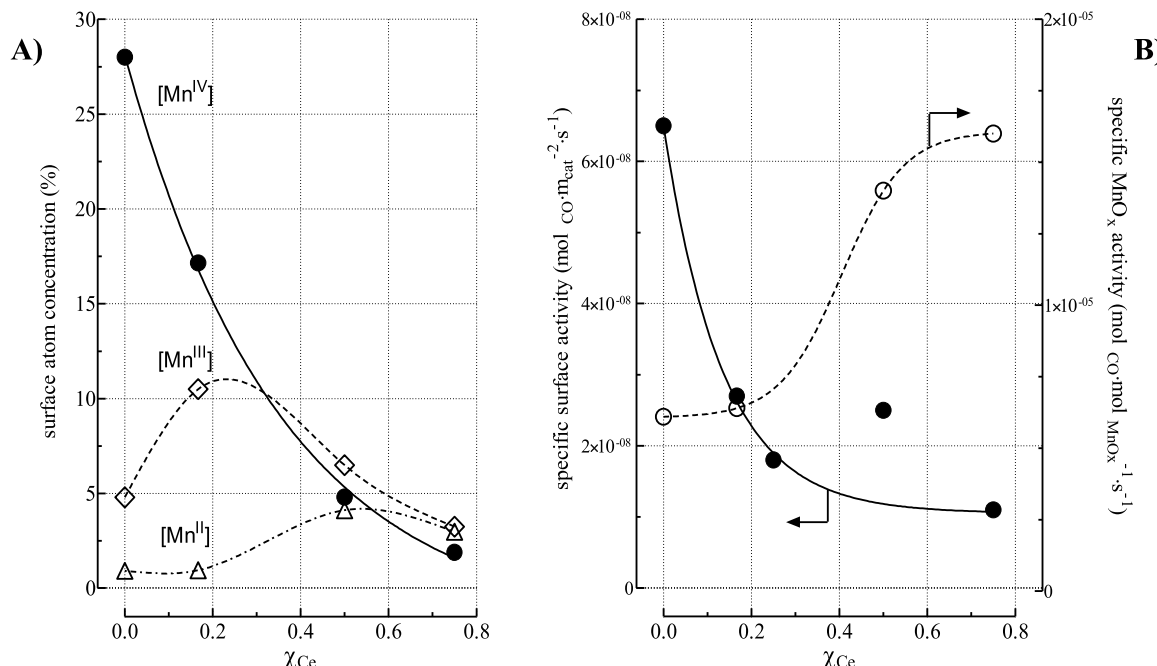
Both analyses provide fairly accurate linear correlations (Fig. S5), resulting in very close E_{app} values for all the studied systems (Table 3). Matching the energetic barrier of the M1C1-R4 catalyst (41 ± 3 kJ/mol) found by isothermal measurements [11], these data (37–47 kJ/mol) rule out any change of reaction mechanism between 353 and 533K, according to literature indicating a Langmuir-Hinshelwood (L-H) path on MnO_x and MnCeO_x systems in that range [11,13–15,22,23,43,44]. Moreover, a similar activation barrier of pure ceria (51–52 kJ/mol) explains the lack of significant chemical effects in composite catalysts, likewise to that observed in the selective oxidation of benzyl alcohol [32]. In turn, this finding indicates that the reactivity of the various catalysts depends on the availability of active sites, the nature of which can be probed by comparing rate values with the surface abundance of the various Mn centers. On this account, a deconvolution analysis of Mn_{2p}/XPS peaks was performed by a linear combination of Shirley-background and Gaussian-Lorentzian model functions centred at 640.5, 641.2, 642.3 and 643.3 eV, associated to II, III and IV states, while the latter was taken for Mn^{IV} ions in KMnO_x species (Fig. S6) [9,23,34,59]. Deconvolution data are summarized in Table 4, while the surface abundance of Mn centers is shown in Fig. 7A. According to AON data, the surface concentration of Mn^{IV}

Table 3Activation energy values (E_{app}) and activity data of the studied catalysts at 393K.

Catalyst	E_{app} ^a (kJ/mol)	E_{app} ^b (kJ/mol)	X_{CO} ^c (%)	rate ^c (mol _{CO} g _{cat} ⁻¹ s ⁻¹)	rate _{MnO_x} ^c (mol _{CO} g _{MnO_x} ⁻¹ s ⁻¹)	rate _{SA} ^c (mol _{CO} m _{cat} ⁻² s ⁻¹)
C	51 ± 1	52 ± 1	—	—	—	—
M1C3	37 ± 1	42 ± 1	4.6	2.3 · 10 ⁻⁶	1.6 · 10 ⁻⁵	1.1 · 10 ⁻⁸
M1C1	38 ± 1	45 ± 1	9.4	4.8 · 10 ⁻⁶	1.4 · 10 ⁻⁵	2.5 · 10 ⁻⁸
M3C1	45 ± 1	47 ± 1	6.4	3.3 · 10 ⁻⁶	5.5 · 10 ⁻⁶	1.8 · 10 ⁻⁸
M5C1	39 ± 1	45 ± 1	8.5	4.3 · 10 ⁻⁶	6.4 · 10 ⁻⁶	2.7 · 10 ⁻⁸
M	43 ± 1	47 ± 1	12.0	6.1 · 10 ⁻⁶	6.1 · 10 ⁻⁶	6.5 · 10 ⁻⁸

^a 3–10% X_{CO} range.^b 3–80% X_{CO} data elaboration by Eq. (3) [Ref. [57]].^c Activity data taken from Fig. 2A.**Table 4**Data of the deconvolution analysis of the Mn_{2p3/2} XPS peak (see Fig. S6).

Catalyst	[Mn ^{II}]		[Mn ^{III}]		[Mn ^{IV}]		[Mn ^{IV}] ^a		AON ^b
	C (eV)	A (%)	C (eV)	A (%)	C (eV)	A (%)	C (eV)	A (%)	
M1C3	640.5	36.7	641.2	40.0	642.3	23.3	—	0.0	2.87
M1C1	640.5	26.7	641.2	42.1	642.3	31.2	—	0.0	3.05
M5C1	640.6	3.3	641.2	36.7	642.3	45.6	643.3	14.4	3.57
M9C1	640.6	3.0	641.2	23.8	642.3	59.4	643.3	13.9	3.70
M	640.6	2.7	641.2	14.2	642.3	50.4	643.3	32.7	3.81

^a Mn^{IV} ions in KMnO_x structures.^b AON=(2 × [Mn^{II}]+3 × [Mn^{III}]+4 × Σ[Mn^{IV}]).Fig. 7. Influence of the cerium loading on: (A) surface concentration of Mn centers; and (B) surface and MnO_x specific activity at 393K.

sites decreases steadily with χ_{Ce} from 30 (M) to 5% (M1C3), while Mn^{III} and Mn^{II} ones depict volcano-shaped trends with maxima of 10 and 5% on M5C1 and M1C1 samples, respectively. Larger Mn^{II} populations likely reflect the formation of surface solid solutions in M1C1 and M1C3 samples [21,23,49].

The studied catalysts feature at 393K a reactivity analogous to M1C1-R4 catalyst [11], even if rate values comprised between 2.3 and 6.1 $\mu\text{mol}_{CO}\text{ g}_{cat}^{-1}\text{ s}^{-1}$ follow an unpredictable trend (Table 3), which is likely consequence of different availability and types of active sites. In fact, these account for a specific surface rate decreasing in a way comparable to Mn^{IV} centers with χ_{Ce} (Fig. 7B), substantiating their role of active sites in bulk and composite catalysts [16,22,43,44,58]. However, further insights into the effects of

cerium on the functionality of composite catalysts come from the specific MnO_x rate values, indicating a threefold higher activity of Mn^{IV} centers in M1C3 and M1C1 catalysts than M5C1 and M ones (Fig. 7B). This peculiar rising trend reveals some chemical effects in composite catalysts with high Ce loading, clearly related to high dispersion and strong oxide-interaction. In fact, this matches the formation of “isolated” Mn^{IV} centers in a strong interaction with ceria featuring a better CO oxidation functionality than MnO₂ nanodomains [9,11,32,34,43,44,49]. In conclusion, structure-activity relationships disclose that different Mn^{IV} sites shape the CO oxidation activity of nanostructured MnCeO_x catalysts, well accounting for the “unusually high” surface reactivity of M1C1 catalyst (Fig. 7B).

4. Conclusions

The effects of Ce addition on the physico-chemical properties and CO oxidation functionality of nanostructured MnCeO_x catalysts are summarized in the followings:

- Cerium induces remarkable structural effects in nanostructured MnCeO_x materials;
- High surface area and oxide dispersion promote the catalyst reducibility;
- The CO oxidation functionality of bulk MnO_x and composite MnCeO_x materials depends on the availability of surface Mn^{IV} centers;
- Composition, surface area, oxide dispersion and interaction strength determine various Mn sites, shaping the reactivity of nanocomposite MnCeO_x catalysts.

Acknowledgements

This work is dedicated to our friend and colleague Prof. Leone Spiccia who passed away on Dec. 18th 2016, leaving a great human and professional void in all of us.

References

- [1] S. Royer, D. Drupe, ChemCatChem 3 (2011) 24–65.
- [2] M.E. Ali, M.M. Rahman, S.M. Sarkar, S.B.A. Hamid, J. Nanomat. (2014) (2014).
- [3] F. Arena, Catal. Sci. Technol. 4 (2014) 1890–1898.
- [4] F. Arena, R. Di Chio, B. Guminia, L. Spadaro, G. Trunfio, Inorg. Chim. Acta 431 (2015) 101–109.
- [5] F. Arena, C. Italiano, L. Spadaro, Appl. Catal. B: Environ. 115–116 (2012) 336–345.
- [6] K.-H. Kim, S.-K. Ihm, J. Hazard. Mater. 186 (2011) 16–34.
- [7] B. Bai, Q. Qiao, J. Li, J. Hao, Chin. J. Catal. 37 (1) (2016) 102–122.
- [8] K. Frey, V. Iablokov, G. Sáfrán, J. Osán, I. Sajó, R. Szukiewicz, S. Chenakin, N. Kruse, J. Catal. 287 (2012) 30–36.
- [9] P. Zhang, H. Lu, Y. Zhou, L. Zhang, Z. Wu, S. Yang, H. Shi, Q. Zhu, Y. Chen, S. Dai, Nat. Commun. 6 (2015) 1–10.
- [10] P. Doggali, Y. Teraoka, S. Rayalu, N. Labhsetwar, J. Environ. Chem. Eng. 3 (2015) 420–428.
- [11] F. Arena, G. Trunfio, B. Fazio, J. Negro, L. Spadaro, J. Phys. Chem. C 113 (7) (2009) 2822–2829.
- [12] M. Tepluchin, M. Casapu, A. Boubnov, H. Leitemberg, D. Wang, S. Kureti, J.-D. Grunwaldt, ChemCatChem 6 (2014) 1763–1773.
- [13] J. Xu, Y.-Q. Deng, Y. Luo, W. Mao, X.-J. Yang, Y.-F. Han, J. Catal. 300 (2013) 225–234.
- [14] J. Xu, Y.-Q. Deng, X.-M. Zhang, Y. Luo, W. Mao, X.-J. Yang, L. Ouyang, P. Tian, Y.-F. Han, ACS Catal. 4 (2014) 4106–4115.
- [15] K. Ramesh, L. Chen, F. Chen, Y. Liu, Z. Whang, Y.-F. Han, Catal. Today 131 (2008) 477–482.
- [16] R. Craciun, B. Nentwick, K. Hadjiivanov, H. Knözinger, Appl. Catal. A: Gen. 243 (2003) 67–79.
- [17] D. Li, J. Yang, W. Tang, X. Wu, L. Wei, Y. Chen, RCS Adv. 4 (2014) 26796–26803.
- [18] K. Morgan, K.J. Cole, A. Goguet, C. Hardacre, G.J. Hutchings, N. Maguire, S.O. Shekhtman, S.H. Taylor, J. Catal. 276 (2010) 38–48.
- [19] J.-H. Park, D.-C. Kang, S.-J. Park, C.-H. Shin, J. Ind. Eng. Chem. 25 (2015) 250–257.
- [20] J. Jia, P. Zhang, L. Chen, Appl. Catal. B: Environ. 189 (2016) 210–218.
- [21] P. Venkataswamy, K.N. Rao, D. Jampaiah, B.M. Reddy, Appl. Catal. B: Environ. 162 (2015) 122–132.
- [22] X.-m. Zhang, Y.-Q. Deng, P. Tian, H.-h. Shang, J. Xu, Y.-F. Han, Appl. Catal. B: Environ. 191 (2016) 179–191.
- [23] Z.-Q. Zou, M. Meng, Y.-Q. Zha, J. Phys. Chem. C 114 (2010) 468–477.
- [24] G. Qi, R.T. Yang, J. Catal. 217 (2003) 434–441.
- [25] G. Qi, R.T. Yang, R. Chang, Appl. Catal. B: Environ. 51 (2004) 93–106.
- [26] Z. Liu, Y. Yi, S. Zhang, T. Zhu, J. Zhu, J. Wang, Catal. Today 216 (2013) 76–81.
- [27] F. Eigemann, M. Maciejewski, A. Baiker, Appl. Catal. B: Environ. 62 (2006) 311–318.
- [28] X. Wang, Y. Zheng, J. Lin, Catal. Commun. 37 (2013) 96–99.
- [29] H. Chang, X. Chen, J. Li, L. Ma, C. Wang, C. Liu, J.W. Schwank, J. Hao, Environ. Sci. Technol. 47 (2013) 5294–5301.
- [30] C. Cannilla, G. Bonura, E. Rombi, F. Arena, F. Frusteri, Appl. Catal. A: Gen. 382 (2010) 158–166.
- [31] C. Cannilla, G. Bonura, F. Arena, E. Rombi, F. Frusteri, Catal. Today 195 (2012) 32–43.
- [32] F. Arena, B. Guminia, A.F. Lombardo, C. Espro, A. Patti, L. Spadaro, L. Spiccia, Appl. Catal. B: Environ. 162 (2015) 260–267.
- [33] F. Arena, B. Guminia, C. Cannilla, L. Spadaro, A. Patti, L. Spiccia, Appl. Catal. B: Environ. 170–171 (2015) 233–240.
- [34] P. Sudarsanam, B. Hillary, M.H. Amin, S.B.A. Hamid, S.K. Bhargava, Appl. Catal. B: Environ. 185 (2016) 213–224.
- [35] L. Delmondo, G.P. Salvador, J.A. Muñoz-Tabares, A. Sacco, N. Garino, M. Castellino, M. Gerosa, G. Massaglia, A. Chiodoni, M. Quaglio, Appl. Surf. Sci. 388 (2016) 631–639.
- [36] K. Selvakumar, S.M.S. Kumar, R. Thangamuthu, K. Ganesan, P. Murugan, P. Rajput, S.N. Jha, D. Bhattacharyya, J. Phys. Chem. C 119 (2015) 6604–6618.
- [37] M. Fekete, R. Hocking, S.L.Y. Chang, C. Italiano, A. Patti, F. Arena, L. Spiccia, Energy Environ. Sci. 6 (2013) 2222–2232.
- [38] F.H.B. Lima, M.L. Calegaro, E.A. Ticianelli, J. Electroanal. Chem. 590 (2006) 152–160.
- [39] F. Arena, G. Trunfio, J. Negro, L. Spadaro, Appl. Catal. B: Environ. 85 (2008) 40–47.
- [40] F. Arena, J. Negro, A. Parmaliana, L. Spadaro, G. Trunfio, Ind. Eng. Chem. Res. 46 (2007) 6724–6731.
- [41] F. Arena, G. Trunfio, J. Negro, B. Fazio, L. Spadaro, Chem. Mater. 19 (2007) 2269–2276.
- [42] F. Arena, L. Spadaro, W.O. 2012168957 (A1) (2012).
- [43] L.-C. Hsu, M.-K. Tsai, Y.-H. Lu, H.-T. Chen, J. Phys. Chem. C 117 (2013) 433–441.
- [44] W. Cen, Y. Liu, Z. Wu, H. Wang, X. Weng, Phys. Chem. Chem. Phys. 14 (2012) 5769–5777.
- [45] F. Larachi, Top. Catal. 33 (2005) 109–134.
- [46] J. Hendrick, D. Cordier, J. Gambogi, Mineral Commodity Summaries – Rare Earths, U.S. Geol. Surv. 1996–2015; http://minerals.usgs.gov/minerals/pubs/commodity/rare_earths/index.html#mcs.
- [47] A. Parmaliana, F. Arena, J. Catal. 167 (1997) 57–65.
- [48] F. Arena, P. Famulari, G. Trunfio, G. Bonura, F. Frusteri, L. Spadaro, Appl. Catal. B: Environ. 66 (2006) 81–91.
- [49] X. Zhang, J. Wei, X. Liu, W. Liu, C. Zhang, Y. Yang, Eur. J. Inorg. Chem. 25 (2013) 4443–4449.
- [50] T. Gao, H. Fjellvag, P. Norby, Anal. Chim. Acta 648 (2009) 235–239.
- [51] B. Fazio, L. Spadaro, G. Trunfio, J. Negro, F. Arena, J. Raman Spectr. 42 (2011) 1583–1588.
- [52] E. Widjaja, J.T. Sampanthar, Anal. Chim. Acta 585 (2007) 241–245.
- [53] Y. Hamiouli, L. Tifouti, C. Remazeilles, F. Pedraza, Mater. Chem. Phys. 120 (2010) 172–180.
- [54] T. Sato, T. Komanoya, Catal. Commun. 10 (2009) 1095–1098.
- [55] X. Wu, S. Liu, D. Weng, F. Lin, R. Ran, J. Hazard. Mater. 187 (2011) 283–290.
- [56] F. Larachi, J. Pierre, A. Adnot, A. Bernis, Appl. Surf. Sci. 195 (2002) 236–250.
- [57] C.-J. Liang, J.-W. Fang, Chem. Eng. Sci. 144 (2016) 101–107.
- [58] F. Arena, R. Di Chio, C. Espro, A. Palella, L. Spadaro, manuscript in preparation.
- [59] M.C. Biesinger, B.P. Payne, A.P. Grovesnor, L.W.M. Lau, A.R. Gerson, R.St.C. Smart, Appl. Surf. Sci. 257 (2011) 2717–2730.